







Optical/X-ray/radio view of Abell 1213: A galaxy cluster with anomalous diffuse radio emission

W. Boschin^{1,2,3} , M. Girardi^{4,6} , S. De Grandi⁵ , G. Riva^{7,8} , L. Ferretti⁹, G. Giovannini^{9,10},
F. Govoni¹¹ , and V. Vacca¹¹ 

¹ Fundación Galileo Galilei – INAF (Telescopio Nazionale Galileo), Rambla José Ana Fernández Perez 7, 38712 Breña Baja (La Palma), Canary Islands, Spain
e-mail: boschin@tng.iac.es

² Instituto de Astrofísica de Canarias, C/Vía Láctea s/n, 38205 La Laguna (Tenerife), Canary Islands, Spain

³ Departamento de Astrofísica, Univ. de La Laguna, Av. del Astrofísico Francisco Sánchez s/n, 38205 La Laguna (Tenerife), Canary Islands, Spain

⁴ Dipartimento di Fisica dell'Università degli Studi di Trieste – Sezione di Astronomia, Via Tiepolo 11, 34143 Trieste, Italy

⁵ INAF – Osservatorio Astronomico di Brera, Via E. Bianchi 46, 23807 Merate, Italy

⁶ INAF – Osservatorio Astronomico di Trieste, Via Tiepolo 11, 34143 Trieste, Italy

⁷ INAF – Istituto di Astrofisica Spaziale e Fisica Cosmica di Milano, Via A. Corti 12, 20133 Milano, Italy

⁸ Dipartimento di Fisica, Università degli Studi di Milano, Via G. Celoria 16, 20133 Milano, Italy

⁹ INAF – Istituto di Radioastronomia, Via P. Gobetti 101, 40129 Bologna, Italy

¹⁰ Dipartimento di Fisica e Astronomia, Università di Bologna, Via Gobetti 93/2, 40129 Bologna, Italy

¹¹ INAF – Osservatorio Astronomico di Cagliari, Via della Scienza 5, 09047 Selargius, Italy

Received 3 January 2023 / Accepted 27 February 2023

ABSTRACT

Context. Abell 1213, a low-richness galaxy system, is known to host an anomalous radio halo detected in data of the Very Large Array (VLA). It is an outlier with regard to the relation between the radio halo power and the X-ray luminosity of the parent clusters.

Aims. Our aim is to analyze the cluster in the optical, X-ray, and radio bands to characterize the environment of its diffuse radio emission and to shed new light on its nature.

Methods. We used optical data from the Sloan Digital Sky Survey to study the internal dynamics of the cluster. We also analyzed archival *XMM-Newton* X-ray data to unveil the properties of its hot intracluster medium. Finally, we used recent data from the LOFAR (LOFAR) at 144 MHz, together with VLA data at 1.4 GHz, to study the spectral behavior of the diffuse radio source.

Results. Both our optical and X-ray analysis reveal that this low-mass cluster exhibits disturbed dynamics. In fact, it is composed of several galaxy groups in the peripheral regions and, in particular, in the core, where we find evidence of substructures oriented in the NE–SW direction, with hints of a merger nearly along the line of sight. The analysis of the X-ray emission adds further evidence that the cluster is in an unrelaxed dynamical state. At radio wavelengths, the LOFAR data show that the diffuse emission is ~ 510 kpc in size. Moreover, there are hints of low-surface-brightness emission permeating the cluster center.

Conclusions. The environment of the diffuse radio emission is not what we would expect for a classical halo. The spectral index map of the radio source is compatible with a relic interpretation, possibly due to a merger in the N–S or NE–SW directions, in agreement with the substructures detected through the optical analysis. The fragmented, diffuse radio emissions at the cluster center could be attributed to the surface brightness peaks of a faint central radio halo.

Key words. galaxies: clusters: individual: Abell 1213 – galaxies: clusters: general – galaxies: clusters: intracluster medium – Galaxy: kinematics and dynamics – acceleration of particles – large-scale structure of Universe

1. Introduction

Radio halos are diffuse, low-surface-brightness synchrotron sources ($\sim 0.1 \mu\text{Jy arcsec}^{-2}$ at 1.4 GHz) hosted in the central volume of a fraction of massive and unrelaxed galaxy clusters. They extend up to spatial sizes of 1–2 Mpc, roughly following the distribution of the intracluster medium (ICM) and have no evident counterparts in the optical band. Their steep spectrum ($S(\nu) \sim \nu^{-\alpha}$; with $\alpha > 1$) indicates the existence in the ICM of ultra-relativistic electrons ($\gamma \gg 1000$) moving in weak ($\sim \mu\text{G}$) magnetic fields (see, e.g., Ferretti et al. 2012; van Weeren et al. 2019 for reviews).

A strong correlation has been found between the total power of radio halos at 1.4 GHz ($P_{1.4\text{GHz}}$) and the X-ray luminosity (L_X) of the ICM (Ferretti et al. 2012; Cassano et al. 2013;

Yuan et al. 2015; Cuciti et al. 2021), but there are notable outliers. In fact, anomalous radio halos have been observed with a radio power larger than expected from the $P_{1.4\text{GHz}}-L_{X,0.1-2.4\text{keV}}$ correlation shown by the majority of radio halos, with the halo in Abell 523 among of the most frequently studied of this type (Girardi et al. 2016; Vacca et al. 2022a,b).

Another controversial case is the diffuse source in the galaxy cluster Abell 1213 (hereafter A1213). This is a poor (Abell richness class = 1; Abell et al. 1989) cluster at $z \sim 0.047$ dominated in its central region by the FR II radio galaxy 4C29.41 and two more cluster members identified as radio galaxies.

Very notably, NE of 4C29.41, data of the NRAO VLA Sky Survey (NVSS; Condon et al. 1998) and observations with the Very Large Array (VLA) at 1.4 GHz by Giovannini et al. (2009; hereafter G09) revealed the presence of a diffuse extended

emission that does not seem due to the discrete radio sources in the cluster central region. Indeed, G09 classified it as a small-size radio halo, concluding that the radio morphology and power of this diffuse source are linked to the physical properties of the cluster as a whole and not to the activity of cluster radio galaxies. However, if this source is a radio halo, it would be really peculiar. In fact, it appears well off-centered with respect to the ICM distribution inferred from ROSAT/HRI data and overluminous when compared to the ICM X-ray luminosity (see Fig. 17 of G09). Moreover, the low X-ray luminosity ($L_X = 0.10 \times 10^{44} \text{ erg s}^{-1}$ in the ROSAT 0.1–2.4 keV band; Ledlow et al. 2003) and poor optical richness of A1213 suggest that it is not massive in comparison with typical clusters known to host a radio halo. An analysis based on redshift data from the Sloan Digital Sky Survey (SDSS) DR6 by Hernández-Fernández et al. (2012) supports this hypothesis. In fact, they measure a member galaxies velocity dispersion of $\sim 560 \text{ km s}^{-1}$ (see their Table 1). This is quite a low value, bearing in mind that massive clusters with radio halos often exhibit velocity dispersions $\geq 1000 \text{ km s}^{-1}$.

In this intriguing context, we performed an exhaustive study of A1213 in the optical, X-ray, and radio bands. In particular, we used SDSS photometric and spectroscopic information to extend the analysis of Hernández-Fernández et al. (2012) by searching for optical substructures, which are an indicator of the dynamical state of the cluster (e.g., Girardi & Biviano 2002). Then, we complemented the optical analysis with public X-ray data from *XMM-Newton* to draw a multiband picture of A1213 and use this information to study the environment of its extended radio emission. Finally, we used archival radio data from the LOFAR and the VLA data by G09 to derive the spectral properties of the diffuse radio source.

The paper is organized as follows. We describe the analyzed optical data and select the members of the cluster in Sect. 2. We estimate the global properties and analyze the optical substructures in Sects. 3 and 4. In Sect. 5, we discuss the large-scale structure around the cluster, while in Sect. 6, we present the analysis and results of the *XMM-Newton* X-ray data. In Sect. 7, we show the radio data from LOFAR. Section 8 is devoted to the summary and discussion of our results. In this work, we use $H_0 = 70 \text{ km s}^{-1} \text{ Mpc}^{-1}$ in a flat cosmology with $\Omega_m = 0.3$ and $\Omega_\Lambda = 0.7$. In the assumed cosmology, $1'$ corresponds to $\sim 55.2 \text{ kpc}$ at the cluster redshift. We recall that the velocities we derive for the galaxies are line-of-sight velocities determined from the redshift, $V = cz$. Unless otherwise stated, we report errors with a confidence level (c.l.) of 68%.

2. Redshift data and spectroscopic cluster members

From SDSS DR13, we extracted 402 galaxies with a redshift $z \leq 0.2$ within a radius $R = 60'$, corresponding to 3.31 Mpc in the cluster rest frame, from the position RA = $11^{\text{h}}16^{\text{m}}40^{\text{s}}00$, Dec = $+29^{\circ}16'00''0$ (J2000).

To select cluster members among the 402 galaxies in the spectroscopic catalog, we used the two-step method known as Peak+Gap (P+G), which was previously applied by Girardi et al. (2015). The first step is the application of the adaptive-kernel DEDICA method (Pisani 1993, 1996; see also Girardi et al. 1996). Using this method, A1213 is identified as a peak at $z \sim 0.04658$ consisting of 144 galaxies in the range $0.041989 \leq z \leq 0.052006$, that is, $12588 \leq V \leq 15591 \text{ km s}^{-1}$ for the line-of-sight velocity $V = cz$ (see Fig. 1). Of the non-member galaxies, 53 are foreground and 205 are background galaxies.

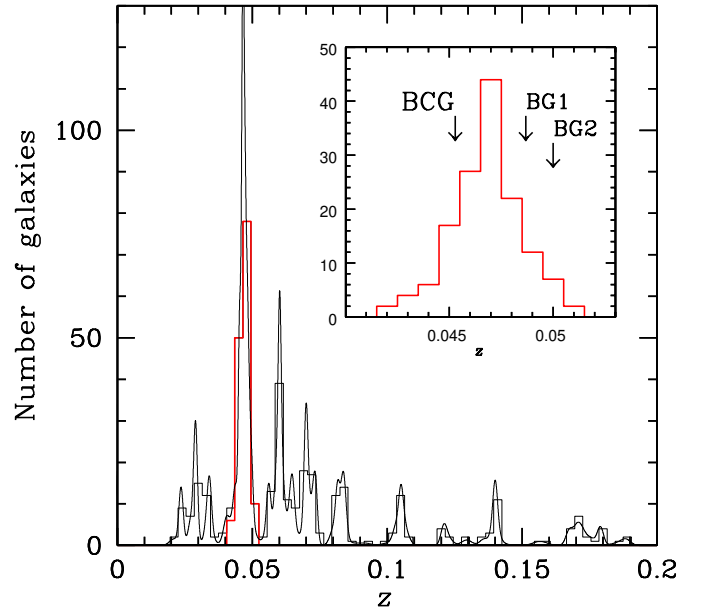


Fig. 1. Distribution of redshifts of galaxies with $z \leq 0.2$. The histogram refers to all galaxies with spectroscopic redshifts in the region of A1213. The histogram with the thick red line highlights the 144 galaxies that are assigned to A1213 using the 1D-DEDICA reconstruction method. The inset shows the final 143 member galaxies, with the redshifts of the BCG and the pair of bright close galaxies BG1 and BG2 shown.

In a second step, we combine the space and velocity information by using the “shifting gapper” method (Fadda et al. 1996; Girardi et al. 1996). Of the galaxies that lie within an annulus around the center of the cluster, this procedure rejects those that are too far away in terms of velocity from the main body (i.e., farther away than a fixed velocity gap). The position of the annulus is shifted with increasing distance from the center of the cluster. The procedure is repeated until the number of cluster members converges to a stable value. Following Fadda et al. (1996), we used a gap of 1000 km s^{-1} in the cluster rest frame and an annulus size of 0.6 Mpc or more to include at least 15 galaxies. In determining the cluster center, we considered the position in right ascension (RA) and declination (Dec) of the brightest cluster galaxy in our sample (BCG) [RA = $11^{\text{h}}16^{\text{m}}22^{\text{s}}70$, Dec = $+29^{\circ}15'08''3$ (J2000)]. With this procedure, one galaxy is discarded and we confirm 143 cluster members. The distribution of member galaxies is shown in the redshift space and in the projected phase space in Figs. 1 and 2, respectively. To highlight the region of cluster members, we also plot in Fig. 2 the escape velocity curves obtained with the mass estimate calculated below (see Sect. 3), assuming a Navarro et al. (1997) mass-density profile and adopting the prescription of den Hartog & Katgert (1996).

Table 1 lists the velocity catalog for the prominent member galaxies. Instead, Fig. 3 shows the central region of the cluster with, superimposed, the VLA radio (from G09) and *XMM-Newton* X-ray contours obtained from our analysis (see Sect. 6).

The cluster galaxy population is dominated by the brightest cluster galaxy (BCG) ID 422, which is $\sim 70''$ far from the centroid of the X-ray emission (see Sect. 6). It is also a bright radio source. However, our catalog lists several galaxies with magnitude $r \leq r_{\text{BCG}} + 1$. Indeed, A1213 is a typical “core” cluster, as classified by Rood & Sastry (1971).

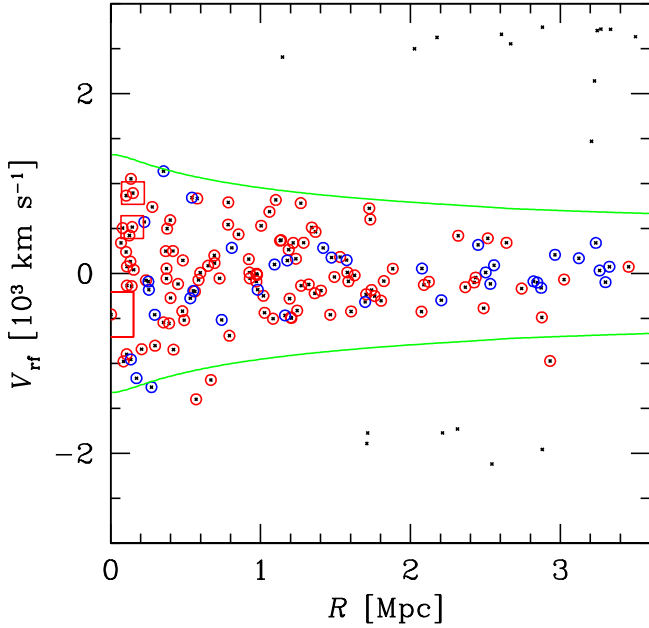


Fig. 2. Projected phase space of the galaxies of A1213, where the rest frame velocity $V_{\text{rf}} = (V - \langle V \rangle)/(1 + z)$ versus the projected cluster-centric distance R is plotted. Only galaxies with redshifts in the range $\pm 3000 \text{ km s}^{-1}$ are shown (black dots). The red and blue circles show the 143 members of the cluster (red and blue galaxies, as defined in the text). The giant and large red squares refer to the BCG and the pair of bright galaxies BG1 and BG2, respectively. The green curves contain the region where $|V_{\text{rf}}|$ is smaller than the escape velocity (see text).

In the central region, the most interesting galaxies are the couple IDs 467+468 (see Fig. 3), very close in the sky and separated by only 400 km s^{-1} in radial velocity. Notably, they show an excess of intracluster light likely due to interaction, thus we treat them as the bright couple BG1+BG2 (see Table 1). If we sum their fluxes we obtain a magnitude $r \sim 13.75$. They have an higher velocity with respect to the average and act as a counterpoint to the BCG (see Fig. 1). We note that ID 467 = BG1 is the optical counterpart of the FR II radio galaxy 4C29.41 (see G09 and Sect. 1).

In Fig. 3, we highlight more notable galaxies. At $\sim 4.6'$ NNE of the BCG, ID 441 is a star-forming spiral galaxy. $\sim 2'$ S of ID 441, ID 442 is an head-tail radio galaxy oriented toward NE. More bright galaxies in Fig. 3 are IDs 408 and 531.

Far from the cluster center, at $\sim 23'$ NW of the BCG (not shown in Fig. 3), ID 274 is a prominent cluster member with a close bright companion. We do not have a spectroscopic redshift for the latter, but the photometric redshift estimate from the SDSS ($z_{\text{phot}} \sim 0.050 \pm 0.009$) suggests it is also a likely cluster member.

3. Global properties and galaxy population

The analysis of the velocity distribution of the 143 cluster members was performed using the biweight estimators for location and scale included in ROSTAT (statistical routines of Beers et al. 1990). Our measurement of the mean redshift of the cluster is $\langle z \rangle = 0.0469 \pm 0.0001$ (i.e., $\langle V \rangle = 14052 \pm 39 \text{ km s}^{-1}$). We estimate the velocity dispersion, σ_V , by applying the cosmological correction and the standard correction for velocity errors (Danese et al. 1980). We obtained a value of $\sigma_V = 463^{+41}_{-31} \text{ km s}^{-1}$, where the errors are estimated by a bootstrap technique.

To derive the mass¹ M_{200} , we used the theoretical relation between the mass M_{200} and the velocity dispersion in clusters presented and verified with simulated clusters by Munari et al. (2013; their Eq. (1) and Fig. 1). We took a recursive approach to this step. To obtain a first estimate of the radius R_{200} and M_{200} , we applied the relation of Munari et al. (2013) to the global value of σ_V obtained above. We considered the galaxies within this first estimate of R_{200} to recalculate the velocity dispersion. The procedure is repeated until a stable result is obtained. We estimated $\sigma_{V,200} = 573^{+52}_{-38}$ for 81 galaxies within $R_{200} = 1.20^{+0.11}_{-0.08} \text{ Mpc}$, in good agreement with the estimate by Hernández-Fernández et al. (2012). The mass is $M_{200} = 2.0^{+0.4}_{-0.6} \times 10^{14} M_{\odot}$. The uncertainty for R_{200} is calculated using the error propagation for σ_V ($R_{200} \propto \sigma_V$), while the uncertainty for M_{200} is computed considering that $M_{200} \propto \sigma_V^3$ and adding an uncertainty of 10% due to the scatter around the relation of Munari et al. (2013). The global properties of the cluster are shown in Table 2.

Figure 4 shows the distribution of member galaxies in the $(r - i \text{ vs. } r)$ and $(g - r \text{ vs. } r)$ color-magnitude diagrams. The $(g - r \text{ vs. } r)$ color-magnitude relation indicating the location of early-type galaxies is seen down to faint magnitudes of $r \sim 17.5 \text{ mag}$, about 2.5 mag fainter than the m_r^* value. Following Boschin et al. (2012) we use a 2σ rejection procedure to obtain $r - i = 0.671 - 0.019 \times r$ and $g - r = 1.378 - 0.037 \times r$. We used the $(g - r \text{ vs. } r)$ relation to classify red and blue galaxies (107 and 36, respectively). Blue galaxies are defined as galaxies that are 0.15 mag bluer than the color expected for their magnitude in the red sequence (i.e., the dashed blue line in Fig. 4, lower panel; e.g., Boschin et al. 2020). Other galaxies are defined as red galaxies.

4. Analysis of optical substructure

We analyzed the presence of substructures using the velocity distribution of galaxies, their projected positions on the sky, and the combination of these two pieces of information (1D, 2D, and 3D tests, respectively).

Using a set of indicators such as kurtosis, skewness, tail index, and asymmetry index (Bird & Beers 1993), the analysis of the velocity distribution shows no evidence of any possible deviations from the Gaussian distribution. The BCG has a lower velocity than the mean velocity of the cluster, and Fig. 1 (inset) shows how much this velocity is peculiar within the velocity distribution. According to the Indicator test by Gebhardt & Beers (1991), the BCG velocity is peculiar at the $>99\%$ c.l.; the same result is obtained when considering the sample of galaxies within R_{200} . For the BCG, we calculate $|V_{\text{rf}}/\sigma_{V,200}| = 0.80$, placing A1213 in the upper range of $|V_{\text{rf}}/\sigma_V|$ distribution, since only about 10% of the clusters have such a high value (see Fig. 8 of Lauer et al. 2014).

Then, we analyzed the spatial 2D distribution of the 143 member galaxies (see Fig. 5). First, we computed the ellipticity (ϵ) and position angle of the major axis (PA, measured counterclockwise from north) using the method based on moments of inertia (Carter & Metcalfe 1980; see also Plionis 2002, where weight equals one). We obtained $\epsilon = 0.24^{+0.06}_{-0.10}$ and $\text{PA} = 119^{+11}_{-10}$. The low value of the ellipticity is due to the complex structure of the cluster rather than a round, homogeneous distribution of galaxies, as shown below.

¹ We refer to R_{Δ} as the radius of a sphere in which the average mass density is Δ times the critical density ρ_c at the redshift of the galaxy system; $M_{\Delta} = (4/3)\pi\Delta\rho_c R_{\Delta}^3$ is the mass contained in R_{Δ} .

Table 1. Prominent member galaxies of A1213.

ID	α, δ (J2000) (h:m:s, °:′:″)	r	V (km s ⁻¹)	ΔV	Comments
422	11 16 22.70, +29 15 08.3	13.64	13 575	4	BCG, radio galaxy
467	11 16 34.61, +29 15 17.2	14.41	14 593	3	BG1, FR II radio galaxy 4C29.41
468	11 16 35.03, +29 14 58.8	14.61	14 988	3	BG2
441	11 16 28.07, +29 19 36.1	13.96	13 863	2	Spiral radio galaxy
274	11 15 10.14, +29 31 48.2	14.11	14 871	3	Far from the center; in substructure 2D–NW
408	11 16 17.41, +29 13 35.1	14.21	13 112	3	
531	11 17 00.39, +29 08 26.2	14.40	13 977	4	
87	11 13 19.44, +29 48 39.9	14.41	13 542	3	In substructure 2D–NW
215	11 14 34.06, +29 32 42.5	14.51	14 031	3	In substructure 2D–NW
442	11 16 28.46, +29 17 09.4	14.64	14 191	4	Head-tail radio galaxy

Notes. Table lists galaxies with magnitude $r \leq r_{\text{BCG}} + 1$. Data from SDSS DR13. Listed: identification number of each galaxy, ID; right ascension and declination, α and δ (J2000); r magnitude; heliocentric radial velocities, $V = cz$, with errors, ΔV ; comments.

We also used the 2D–DEDICA method (Pisani 1996, see also Girardi et al. 1996). Our results are shown in Fig. 5 and Table 3. For each detected galaxy clump with a c.l. greater than 99% and a relative density (with respect to the densest peak) $\rho \gtrsim 0.2$, Table 3 lists the number of member galaxies, the position of the 2D density peak, and ρ . Figure 5 shows the main peak in the cluster core (2D–CORE in Table 3) and two peaks in the NW and NE (2D–NW and 2D–NE) external regions of the cluster (at $R \sim R_{200}$). The BCG is contained in the cluster core, while the NW peak is dominated by the luminous galaxy ID 274 and a close bright likely cluster member (see Sect. 2). The NE peak follows the direction of the main elongation of the X-ray isophotes (see Sect. 6). For all groups, Table 3 also lists the mean velocities, which do not significantly differ taking into account the relative uncertainties. We note that the velocity of the BCG is peculiar with respect to the velocity distribution in the 2D–CORE clump at the 99% c.l.

In the full 3D analysis, we looked for a correlation between velocity and position data. The eventual presence of a velocity gradient is quantified by a multiple linear regression fit to the observed velocities with respect to galaxy positions in the plane of the sky (see also den Hartog & Katgert 1996). To assess the significance of this velocity gradient, we performed 1000 Monte Carlo simulations of galaxy clusters by randomly shuffling the velocities of the galaxies and determining, for each simulation, the coefficient of multiple determination (RC^2 , NAG Fortran Workstation Handbook 1986). The significance of the velocity gradient is the fraction of cases in which the RC^2 of the simulated data is smaller than the observed RC^2 . In A1213, the velocity gradient is not significant in the whole sample as well as within the R_{200} region. Within the $0.5 R_{200}$ region, the velocity gradient is significant at the 98% confidence level. In this case, the position angle on the celestial sphere is $\text{PA} = 33^{+12}_{-16}$ degrees, which means that the high-velocity galaxies are located in the NE region of the cluster (see Fig. 6).

We then used our modified version of the Δ -test of Dressler & Shectman (1988), which considers only the indicator of local mean velocity (hereafter DSV test, Girardi et al. 2016). This indicator is $\delta_{i,V} = [(N_{\text{nn}} + 1)^{1/2} / \sigma_V] \times (V_{\text{loc}} - \langle V \rangle)$, where the local mean velocity V_{loc} is calculated using the i th galaxy and its $N_{\text{nn}} = 10$ neighbors. For a cluster, the cumulative deviation is given by the value of Δ , which is the sum of the $|\delta_{i,V}|$ values of the individual N galaxies. As in the calculation of the velocity gradient, the significance of the Δ (i.e., the presence of substructure)

is based on 1000 Monte Carlo simulated clusters. In A1213, the significance of the substructure is 96.3%. In Fig. 6, we show the Dressler & Shectman bubble-plot resulting from the indicator of the DSV test for the whole sample. Larger circles indicate galaxies where the local mean velocity deviates more from the global velocity. The visual inspection of the bubble plot suggests the presence of poorly populated substructures in the core, in particular, a low-velocity substructure in the SW (large blue circles) and possibly a high-velocity substructure in the NE (large red circles). The relative position of these substructures is consistent with our estimate of the PA of the velocity gradient in the central cluster region.

As an attempt to detect substructure members, we resorted to the technique developed by Biviano et al. (2002). We compared the distribution of $\delta_{i,V}$ values of the real galaxies with the distribution of $\delta_{i,V}$ values of the galaxies of all the 1000 Monte Carlo simulated clusters (Fig. 7). The distribution of values of real galaxies shows a tail at low $\delta_{i,V}$ values and possibly a tail at high $\delta_{i,V}$ values. Looking at galaxies with $|\delta_{i,V}| \gtrsim 3$, we found five galaxies in the low tail and four galaxies in the high tail, with none of them being a luminous galaxy or a galaxy that belongs to the prominent galaxies (Sect. 2).

Since the substructures seem to consist of few galaxies, we repeated the DSV test with $N_{\text{nn}} = 5$ neighbors. The significance of the substructure is 96.6% for the whole sample. If we consider only red passive galaxies, which usually trace the most important structures and merger remnants, the significance increases to 98.3%. In Fig. 8, we show the Dressler & Shectman bubble-plot obtained for the sample of red galaxies. We confirm the presence of a low-velocity poorly populated substructure in the core.

Finally, we used the 3D–DEDICA method (Pisani 1996; Bardelli et al. 1998), which splits A1213 into more than ten groups. Since it is well known that the multidimensional application of the DEDICA algorithm could lead to spurious substructure (Bardelli et al. 1998), we also applied the alternative version of Balestra et al. (2016), based on the rule of thumb for the kernel size given by Silverman (1986). The goal here is to identify the most important substructures at the expense of losing some smaller substructures. Table 4 lists the properties of all the galaxy peaks detected with a probability higher than the >99% c.l. and a relative density $\rho \geq 0.2$. Figure 9 shows the positions of the galaxies associated with the detected peaks. The galaxies assigned to the 3D–NW and 3D–SE peaks form the main system and have similar mean velocities, i.e., they are proba-

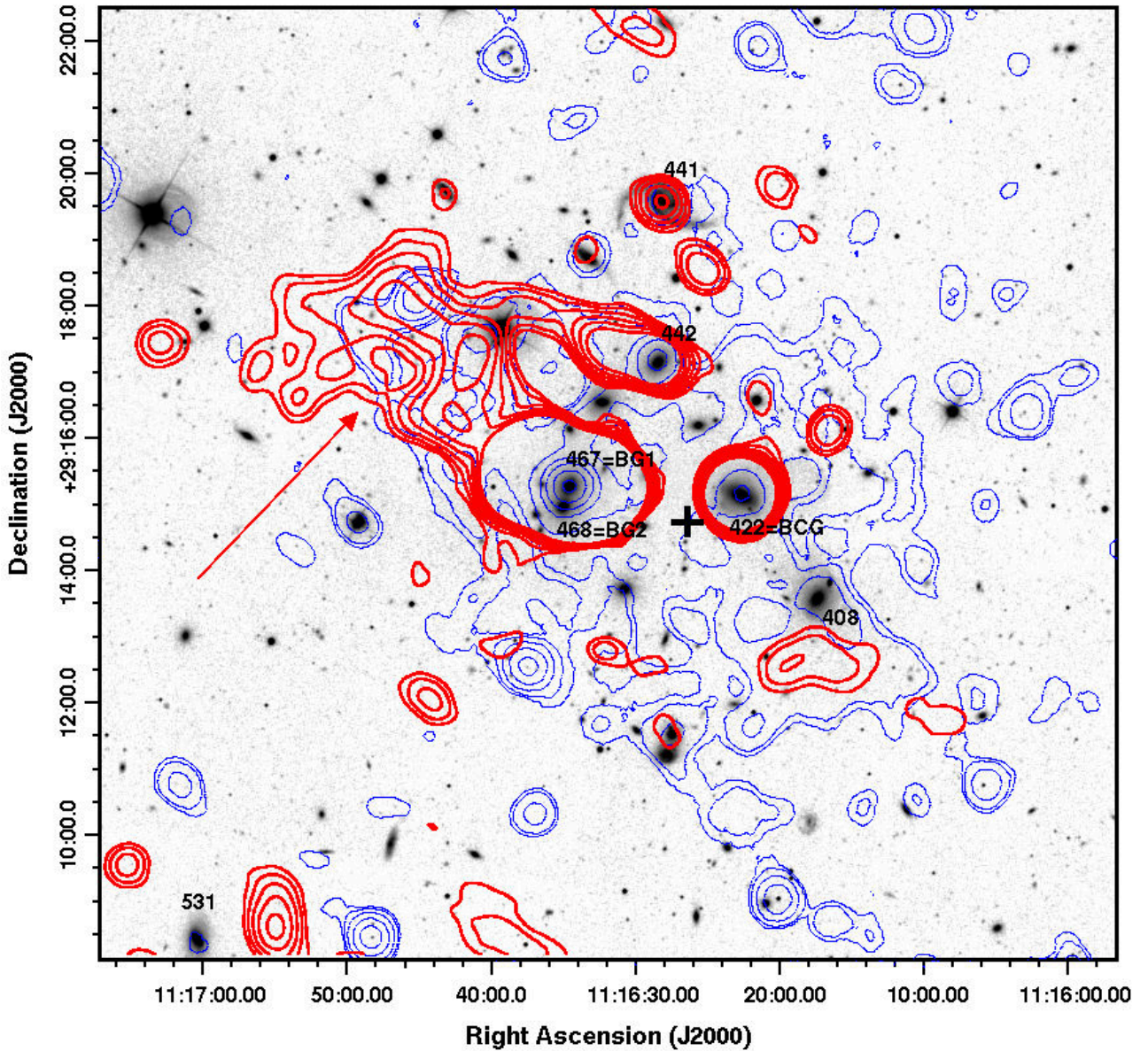


Fig. 3. SDSS g -band image of the galaxy cluster A1213 with, superimposed, the contour levels of the VLA 1.4 GHz radio image by G09 (red thick contours, HPBW = $35'' \times 35''$, first contour level at 1 mJy beam^{-1} , the others spaced by a factor $\sqrt{2}$). Thin blue contours show the (smoothed) X-ray emission of the cluster as derived from the *XMM-Newton* archival image ID 0550270101 (photons in the energy range 0.7–1.2 keV). Labels denote galaxies discussed in the text. The arrow highlights the diffuse radio emission classified by G09 as a small-size radio halo. The black cross shows the position of the centroid of the X-ray emission (see Sect. 6).

bly split because of their different 2D positions. The 3D-CORE peak is a further confirmation of the existence of a group with low-velocity galaxies and projected onto the core.

5. Large scale structure around A1213

From our analysis of the redshift distribution (see Fig. 1), the second peak in relative density is at $z \sim 0.06$ and it is populated by 47 galaxies. Using the 2D-DEDICA method, we find that part of its galaxy population (14 galaxies) clumps together at ESE around the coordinates RA = $11^{\text{h}}19^{\text{m}}35^{\text{s}}00$, Dec = $+29^{\circ}09'48''.7$ (J2000; see Fig. 10). For this group of 14 galaxies, we estimate a velocity dispersion of $\sigma_v \sim 300 \text{ km s}^{-1}$ and $\langle z \rangle = 0.0601$.

The redshift difference between A1213 and this group may be interpreted as a luminosity distance of 61 Mpc or that the group is moving at $V_{\text{rf}} \sim 4000 \text{ km s}^{-1}$ with respect to the

A1213 cluster frame. This speed is of the order of the core-core falling speed in massive clusters. Since A1213 is a poor cluster, we think they are not gravitationally interacting. Moreover, the group is located at $42'$ from the center of A1213, i.e. at a projected distance $>2 \text{ Mpc}$. Also, we note that the color $g-r$ of the group galaxies is slightly redder than the color of red-sequence galaxies of A1213 (see Fig. 4), which is another hint that the group is in the background with respect to A1213.

According to NED², the center of the background group coincides with WHL J111934.5+291100 (also MSPM 02054), at $z \sim 0.059$. We note that at $\sim 40'$ SSW of A1213, an handful of galaxies (see Fig. 10) defines the galaxy group MSPM

² The NASA/IPAC Extragalactic Database (NED) is operated by the Jet Propulsion Laboratory, California Institute of Technology, under contract with the National Aeronautics and Space Administration.

Table 2. Global properties of A1213 as inferred from the analysis of the optical data.

N_{gal}	143
$^{(a)}\alpha, \delta$ (J2000)	11:16:22.70, +29:15:08.3
$\langle V \rangle$ (km s $^{-1}$)	14052 ± 39
σ_V (km s $^{-1}$)	463^{+41}_{-31}
$N_{\text{gal}} (<R_{200})$	81
$\sigma_{V,200}$ (km s $^{-1}$)	573^{+52}_{-38}
R_{200} (Mpc)	$1.20^{+0.11}_{-0.08}$
M_{200} ($10^{14} M_{\odot}$)	$2.0^{+0.6}_{-0.4}$

Notes. $^{(a)}$ As an optical center, we list the position of the BCG.

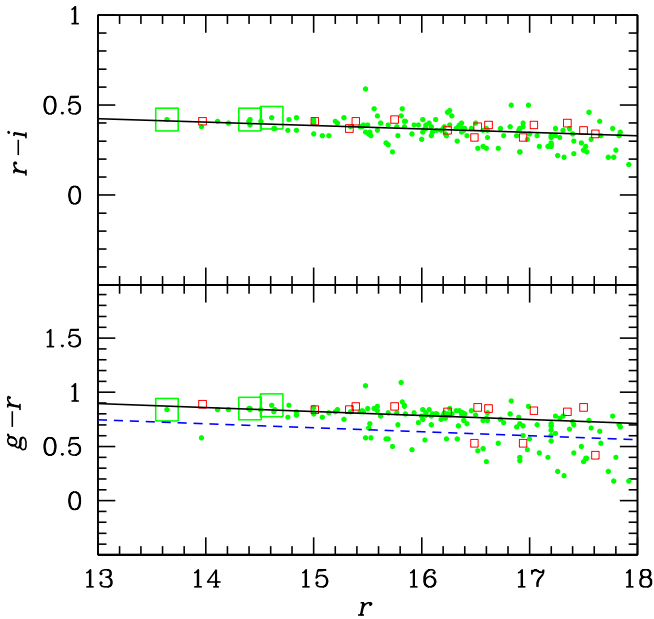


Fig. 4. PanSTARRS magnitude diagrams: $r-i$ vs. r (upper panel) and $g-r$ vs. r (lower panel) of member galaxies of A1213 (green points) and the background eastern group (red squares, see Sect. 5). Large green squares show the BCG and the pair of bright galaxies: BG1 and BG2. Black lines show the color-magnitude relations obtained for the A1213 member galaxies. The blue dashed line in the lower panel is used to separate red galaxies from blue ones.

02299 ($z \sim 0.061$, from NED). At 1.4° SW of A1213 (not shown in Fig. 10), Abell 1185 is the most outstanding structure in the surroundings. According to Einasto et al. (2001), A1213 and Abell 1185 (at $z \sim 0.033$) do not belong to the same supercluster.

6. Analysis of the X-ray data

A1213 was observed by the European Photon Imaging Camera (EPIC, Turner et al. 2001) instrument on board the *XMM-Newton* satellite. EPIC is formed of three detectors MOS1, MOS2, and pn that simultaneously observe the same target. The archival observation was pointed on the radio galaxy 4C29.41, whose optical counterpart is ID 467 = BG1 (obs. ID 0550270101). We reprocessed the dataset using the Extended-Science Analysis System (ESAS, Snowden et al. 2008) embedded in SAS version 16.1 following the analysis described in detail in Ghirardini et al. (2019). After the soft protons cleaning procedure (with the *mos-filter* and *pn-filter* ESAS tasks;

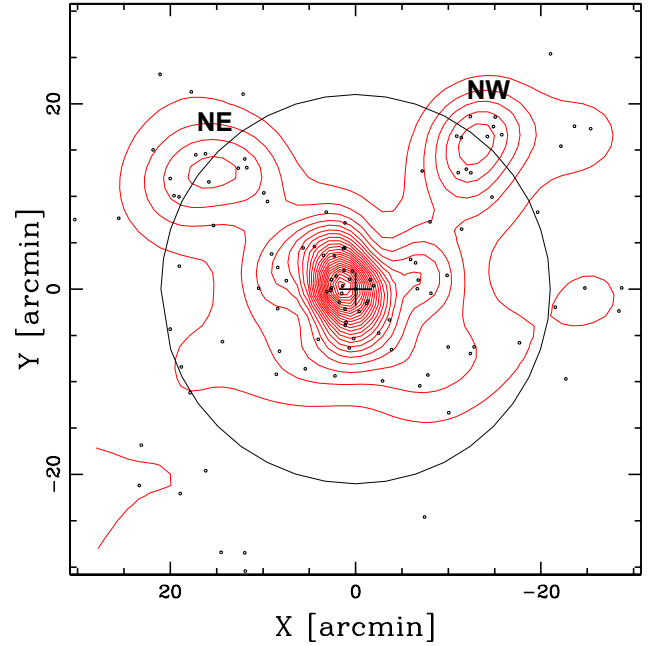


Fig. 5. Spatial distribution in the plane of the sky of the cluster members (black dots) with the corresponding isodensity contour map obtained with the 2D-DEDICA method (red contours). The black cross shows the position of the BCG, which is considered to be the center of A1213. The diagram is centered on the center of the cluster. A circle with a radius of $21'$, i.e., approximately R_{200} , is drawn. The labels refer to the two peripheral 2D-DEDICA peaks listed in Table 3.

Table 3. Optical substructures detected with 2D-DEDICA.

Group	N_{gal}	α, δ (J2000) (h:m:s, °:':")	ρ	$\langle V \rangle$ (km s $^{-1}$)
2D-CORE	56	11 16 29.2+29 15 26	1.00	14045 ± 88
2D-NW	23	11 15 22.8+29 30 55	0.22	13981 ± 61
2D-NE	20	11 17 33.8+29 27 46	0.17	14129 ± 112

Snowden et al. 2008), the total available clean exposure time is 16.5 ks for MOS1, 14.8 ks for MOS2, and 4.3 ks for pn.

We extracted, for each EPIC detector, the photon-count images in the 0.7–1.2 keV band, which is the energy band that maximizes the source-to-background ratio in galaxy clusters (e.g., Ettori et al. 2010), and co-added them to obtain a total EPIC image. With the ESAS tool *eexpmap*, we produced the EPIC exposure map folding the vignetting effect. We used the ESAS collection of closed-filter observations to produce a map of the non-X-ray background (NXB), which we rescaled to our observations by comparing the count rates in the unexposed corners of the field of view. Figure 11 shows the resulting vignetting-corrected, NXB-subtracted, count rate image of A1213. A Gaussian filter smooths the image for visual purposes only.

6.1. X-ray properties of A1213

We performed a spectral analysis of A1213 following the analysis described in Ghirardini et al. (2019). For each region, we extracted spectra and response files using the ESAS tasks *mos-spectra* and *pn-spectra*. From the spectra we filtered out the point

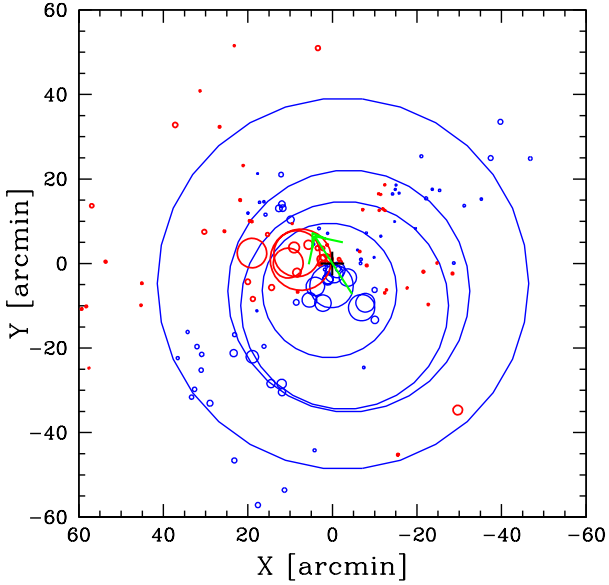


Fig. 6. Dressler & Schectman bubble plot for the DSV test. Spatial distribution of the 143 cluster members, each indicated by a symbol: the larger the symbol, the larger the deviation $|\delta_{i,v}|$ of the local mean-velocity from the global mean-velocity. The blue thin and red thick circles indicate where the local mean velocity is smaller or larger than the global mean velocity. Here the bubble size is less enhanced than the standard size for better readability (size equal to $\exp(w/3)$, with $w = |\delta_{i,v}|$). The green arrow indicates the position angle of the velocity gradient that is calculated within $0.5 R_{200}$. The diagram is centered on the BCG.

sources detected in the field of view by running the SAS wavelet detection tool *ewavdetect* (see Fig. 12).

Since the surface brightness of cluster A1213, apart from some bright point sources, appears to be very shallow, following Leccardi & Molendi (2008) and Ghirardini et al. (2019) we preferred to model the background instead of subtracting it. This approach models the background with different spectral components: (a) the NXB component and (b) the sky-background component, estimated from the region shown in red in Fig. 11 (see Ghirardini et al. 2019 for a detailed explanation of both components).

To estimate the global properties of A1213 we extracted a spectrum from a circle with 5 arcmin radius (shown in white in Fig. 11) centered on the centroid of the X-ray emission (RA = $11^{\text{h}}16^{\text{m}}26^{\text{s}}.40$, Dec = $+29^{\circ}14'46''.8$) within a $5'$ ($\sim 0.4 R_{500}$) radius. We modeled the diffuse source emission with the thin-plasma emission code APEC (Smith et al. 2001) in XSPEC v12.9.1, leaving temperature, metal abundance, and normalization as free parameters (the solar abundances were taken from Asplund et al. 2009) and redshift fixed to the optical value of $z = 0.0469$ (see Sect. 3). This component is absorbed by the Galactic hydrogen column density along the line of sight, which we fixed to the HI4PI Map value ($N_{\text{H}} = 1.19 \times 10^{20} \text{ cm}^{-2}$; Ben Bekhti et al. 2016). We found a best-fit temperature $T_{\text{X}} = 2.02 \pm 0.09 \text{ keV}$ and a metal abundance $Z = 0.26 \pm 0.05$ in solar units (C-Statistic = 1699.93 using 1659 PHA bins and 1653 d.o.f.).

From the scaling relation reported in Arnaud et al. (2005, their Eq. (2)) and the computed mean cluster temperature, we estimated the masses $M_{500} = (1.12 \pm 0.15) \times 10^{14} M_{\odot}$ and $M_{200} = (1.54 \pm 0.25) \times 10^{14} M_{\odot}$, from which we derived $R_{500} = 0.72 \pm 0.03 \text{ Mpc} \sim 12.7'$ and $R_{200} = 1.09 \pm 0.07 \text{ Mpc} \sim 19.2'$. The

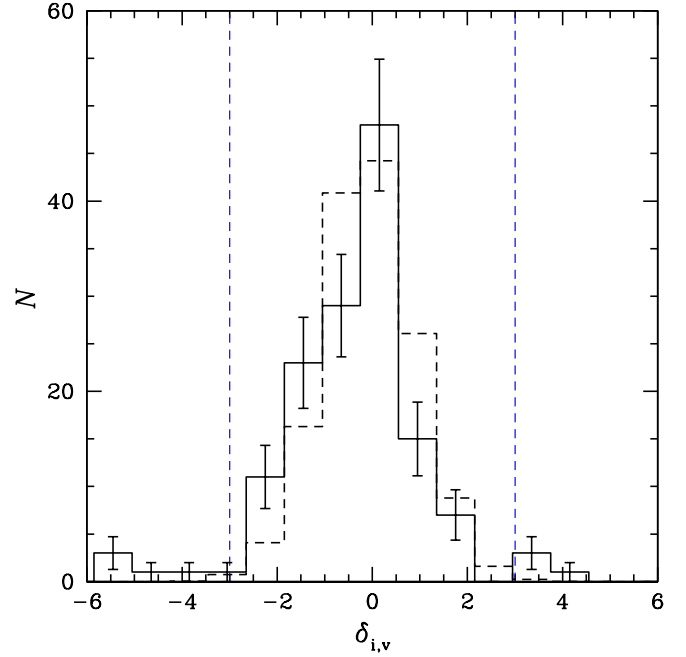


Fig. 7. Distribution of $\delta_{i,v}$ values of the deviation of the local mean velocity from the global velocity (according to the DSV test, see text). The histogram with the solid line shows the observed galaxies. The histogram with the dashed line shows the galaxies of the simulated clusters, normalized to the number of observed galaxies. The blue vertical lines indicate the $|\delta_{i,v}| > 3$ regions where we expect to find substructure members.

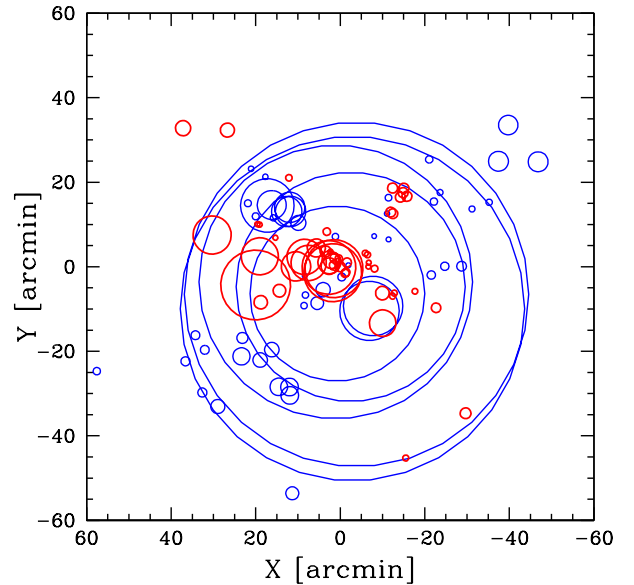


Fig. 8. Dressler & Schectman bubble plot for the DSV test (see also Fig. 6) applied to the red galaxy population only and looking for small substructures ($N_{\text{nn}} = 5$). Here, the bubble size follows the traditional exponential scale (size equal to $\exp(w)$, with $w = |\delta_{i,v}|$).

values of R_{200} and M_{200} estimated from the X-ray measurements are in agreement within errors with those derived from the optical properties (see Tables 2 and 5).

Finally, we extracted the surface brightness (SB) profile of the cluster up to $14'$ and then we fitted the profile with a single β -model, $I(R) = I_0[1 + (R/R_c)^2]^{-3\beta+0.5} + b$ (Cavaliere & Fusco-Femiano 1976), where I_0 , R_c , β and b are

Table 4. Optical substructures detected with 3D-DEDICA.

Group	N_{gal}	V_{peak} (km s^{-1})	α, δ (J2000) (h:m:s, °:′:″)	ρ
3D-NW	107	13 985	11 16 20.2+28 17 31	1.00
3D-SE	26	13 868	11 18 15.7+29 51 43	0.25
3D-CORE	10	13 158	11 16 21.9+29 12 43	0.23

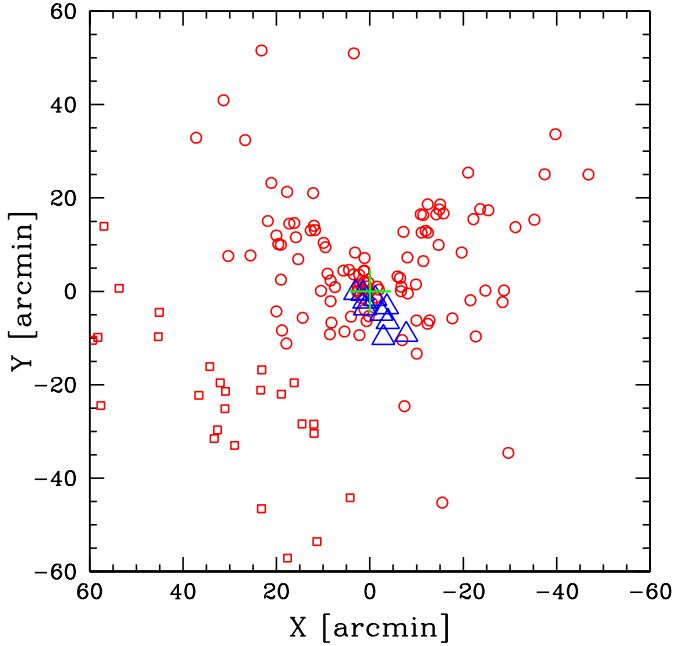


Fig. 9. Spatial distribution of the 143 cluster members in the sky, with the groups discovered with the 3D-DEDICA method marked by different symbols. Red circles and squares show the galaxies of 3D-NW and 3D-SE peaks, respectively. Blue triangles indicate the galaxies of the 3D-CORE peak, which are characterized by low velocities. The green central cross indicates the position of the BCG.

the central surface brightness, core radius, slope, and sky background level, respectively. The extended emission to the north of the cluster, visible in Fig. 11, has been excluded from the extraction of the SB profile. Our best fit gives $\beta = 0.69 \pm 0.20$, $R_c = 4.8 \pm 1.2$ arcmin, $\text{Log}(I_0) = -2.77 \pm 0.03$ and $\text{Log}(b) = -3.76 \pm 0.13$ (I_0 and b in units of $\text{counts s}^{-1} \text{arcmin}^{-2}$, $\chi^2/\text{d.o.f.} = 65.8/38$). The SB profile and the best fit model are plotted in Fig. 13. This result allowed us also to reconstruct the X-ray luminosity of the cluster. In particular, using the *pyproffit.deproject* module (Eckert 2016, 2020), we computed the luminosity within R_{500} . We obtained $L_X [0.1-2.4 \text{ keV}] = (1.53 \pm 0.08) \times 10^{43} \text{ erg s}^{-1}$.

By using the *pyproffit.deproject* module, we also reconstructed the proton density profile (n_p) of the ICM. Remembering that n_p is related to the electron density profile by $n_e = 1.17 n_p$ (Ghirardini et al. 2019), for the central electron density, we obtained a value of $n_{e,0} = 1.19^{+0.43}_{-0.26} \times 10^{-3} \text{ cm}^{-3}$. Govoni et al. (2017) found a scattered correlation between $n_{e,0}$ and the mean central magnetic field strength $\langle B_0 \rangle$ (see their Fig. 15, right panel). This allows us to provide a rough estimate of the magnetic field in the central region of the cluster. We find $\langle B_0 \rangle \sim 2-3 \mu\text{G}$.

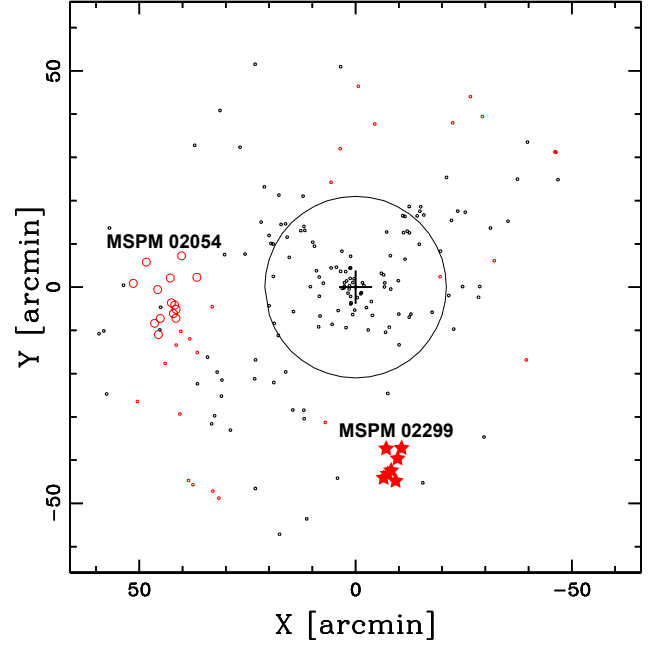


Fig. 10. Spatial distribution of the 47 galaxies populating the redshift peak at $z \sim 0.06$ (red symbols). The galaxies highlighted by red circles are assigned to the eastern clump by 2D-DEDICA, while red stars put in evidence galaxies belonging to the group MSPM 02299 (see text). Black points are the 143 members of A1213, whose BCG is indicated by a black cross. A circle with a radius of $21'$ ($\sim R_{200}$) is also drawn.

6.2. The group at NNW

Figure 11 also shows an extended X-ray emission at $\sim 9'$ NNW of A1213 and centered on the SDSS galaxy CGCG 156-041 (RA = $11^{\text{h}}16^{\text{m}}14^{\text{s}}33$, Dec = $+29^{\circ}23'06''.9$). The galaxy is at $z = 0.02929$, so it is the main member of a foreground system, not related to A1213. We extracted a spectrum from a circular region of $1.5'$ around this galaxy (plotted in magenta in Fig. 11) to estimate the physical properties of this foreground source. For the source emission, we used again the APEC model fixing the metal abundance at $Z = 0.25$ (solar units), $z = 0.02929$, and $N_{\text{H}} = 1.22 \times 10^{20} \text{ cm}^{-2}$. The temperature of the source is $0.83 \pm 0.06 \text{ keV}$, corresponding to a small group of galaxies with a mass $M_{500} \sim 0.2 \times 10^{14} M_{\odot}$ (from the $M_{500}-T_X$ relation in Lovisari et al. 2021).

7. LOFAR radio data

The field of A1213 is covered by the LOw-Frequency ARray (LOFAR) Two-metre Sky Survey (LoTSS-DR2; Shimwell et al. 2022). These data are public (Mosaic Field: P168+30) and provide a picture of the cluster region at 144 MHz, a lower frequency with respect to the VLA data of G09. As shown first by Hoang et al. (2022), the LOFAR images confirm the existence of the diffuse emission observed in NVSS and VLA data. In particular, at 144 MHz the radio emission extends toward the east, with a projected size of $\sim 510 \text{ kpc}$, quite longer than the size of the emission seen by G09 at 1.4 GHz (see Fig. 14). However, we also point out that some fragmented diffuse emission is detected at the cluster center at the 3.3σ level. In particular, there are hints of faint diffuse structures toward NW and SE of the BCG, to the N of the tailed radio galaxy (ID 442) and to the SSE of 4C29.41.

The existence of data sets at two different frequencies allowed us to produce a spectral index map. Indeed,

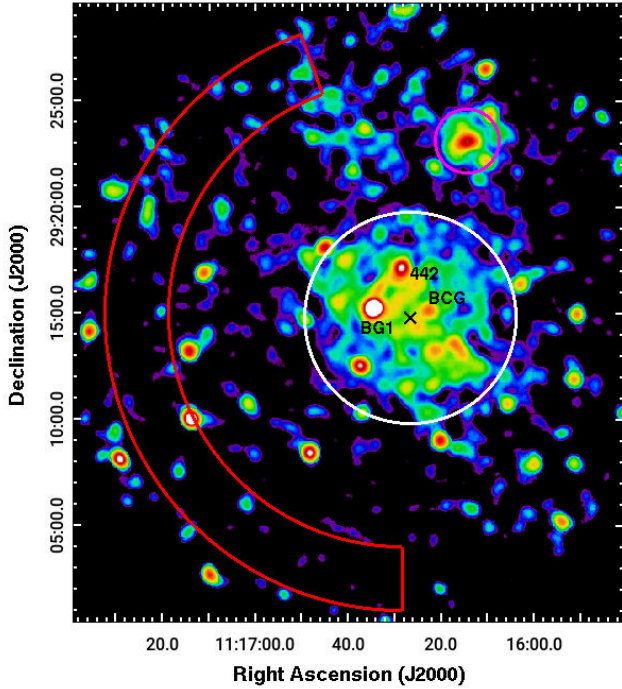


Fig. 11. Smoothed, vignetting-corrected *XMM-Newton*/EPIC count-rate image of A1213 in the 0.7–1.2 keV band. The circles show the regions used to estimate the global X-ray properties of A1213 (white) and of the extended source located NNW of the cluster (magenta, see text). Instead, the red region was used to estimate the local background components. The black cross marks the centroid of the X-ray emission. Black labels highlight galaxies that are also X-ray point sources.

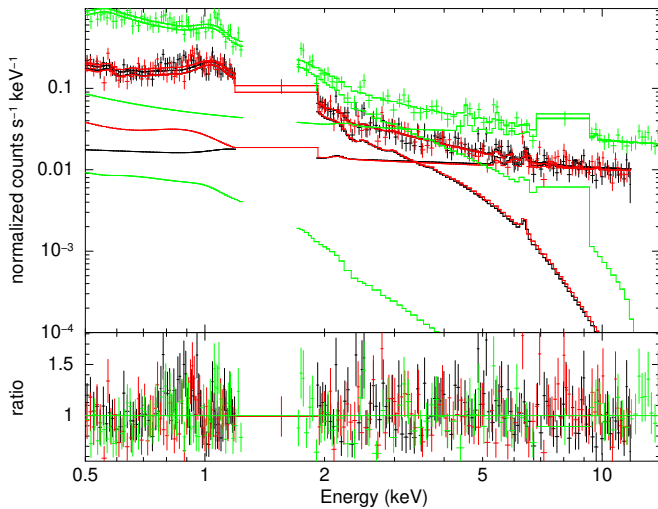


Fig. 12. EPIC spectrum of A1213 extracted from the white circle shown in Fig. 11. The circle has a radius of $5'$. Black points are MOS1, red points MOS2, and green points pn detector data. The lines are the best-fit sky background and source models for the three EPIC detectors. The data around 1.5 keV and 7 keV are excluded from the analysis to avoid strong instrumental line emissions (see Ghirardini et al. 2019). The bottom panel shows the data divided by the folded model.

spatially resolved spectral index mapping of diffuse sources can provide useful information on their nature and origin (e.g., van Weeren et al. 2019).

To produce the spectral index image, we retrieved the LoTTS-DR2 image at the resolution of $20''$ from the Mosaic Field P168+30 (see above) and compared it with the image

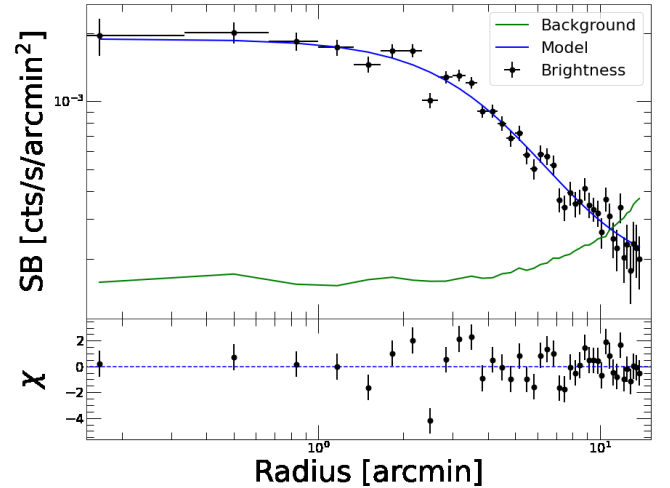


Fig. 13. X-ray surface brightness profile of A1213 (black dots). The blue curve represents the best fit, using a single β model, as described in the text. The particle background (shown as the green curve) has already been subtracted from the X-ray surface brightness profile. The bottom panel shows the contribution of each bin to χ^2 .

Table 5. Global properties of A1213 as inferred from the analysis of the X-ray data.

T_X (keV)	2.02 ± 0.09
$^{(a)}\alpha, \delta$ (J2000)	11:16:26.40, +29:14:46.8
Z (solar units)	0.26 ± 0.05
R_{500} (Mpc)	0.72 ± 0.03
M_{500} ($10^{14} M_\odot$)	1.12 ± 0.15
R_{200} (Mpc)	1.09 ± 0.07
M_{200} ($10^{14} M_\odot$)	1.54 ± 0.25
L_X [0.1–2.4 keV] ($<R_{500}$, 10^{43} erg s $^{-1}$)	1.53 ± 0.08

Notes. $^{(a)}$ Centroid of the cluster X-ray emission.

obtained from the VLA data of G09. In particular, the VLA image was obtained combining C and C/D configuration data (see G09 for more details) using the same cell-size and resolution of the LOFAR image. The two images were put on the same reference frame using the AIPS³ task HGEOM and convolved to the resolution of $40''$ to have a better signal-to-noise ratio in the faint diffuse emission regions. The noise level in the 144 MHz image is 0.28 mJy beam $^{-1}$ and at 1.4 GHz is 0.25 mJy beam $^{-1}$ in the region of A1213. A clip at the 3σ level was applied in producing the spectral index image to avoid large uncertainties. Our map (see Fig. 15) has small uncertainties on the spectral index, mainly in the range 2–12% across the source and indicates a steepening of the radio spectrum from the north to the south of the diffuse emission. In particular, a slice in N–S of this region shows that the spectral index drops from -1.0 ± 0.04 to -1.4 ± 0.04 . This steepening is further highlighted by comparing the average values of the spectral index in the northern and southern regions of the diffuse emission.

We are aware that the LOFAR data provide a better coverage in the short spacing range than the VLA data. However, we note that in the VLA configuration adopted by G09 there are 10 inner antennas in D configuration and the largest structure

³ AIPS is produced and maintained by the National Radio Astronomy Observatory, a facility of the National Science Foundation operated under cooperative agreement by Associated Universities, Inc.

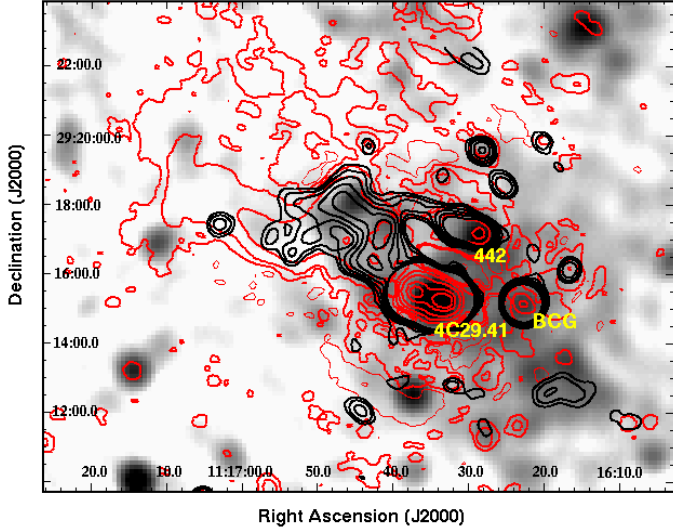


Fig. 14. LOFAR Radio contours of the diffuse radio emission in A1213 at 144 MHz (red, HPBW = $20'' \times 20''$, noise level is $0.15 \text{ mJy beam}^{-1}$, thin contour levels at $-0.5 \text{ mJy beam}^{-1}$, thick contour levels at 0.5, 2, 8, 32, 128, and $1024 \text{ mJy beam}^{-1}$) and VLA contours at 1.4 GHz (black, as in Fig. 3), superimposed to the smoothed *XMM-Newton* image in the energy band 0.7–1.2 keV. Yellow labels highlight prominent galaxies mentioned in the text.

that can be imaged at high sensitivity is $16.2'$ in size. The diffuse emission detected with LOFAR is $\sim 13' \times 9'$ in size, significantly smaller than $16.2'$. Moreover, the size of the structure where we derived the spectral index distribution is even much smaller. Therefore, we are confident that the spectral comparison is not affected by the different uv-coverage (for a similar case see, e.g., Ferretti et al. 2004).

The steepening of the radio spectrum in the N–S direction suggests that this source, rather than a radio halo, could be a radio relic. In fact, this spectral behavior has been observed in confirmed radio relics for which spectral index maps are available (e.g. in the cluster CIZA J2242.8+53.01; van Weeren et al. 2010).

It is known that the properties of relics are related to the X-ray properties of their parent clusters (e.g., Ferretti et al. 2012). This fact offers a way to compare the suspected relic of A1213 with the radio relics known in the literature. The comparison is shown in Fig. 16, which reports the power of radio relics at 1.4 GHz versus the X-ray luminosity of the parent clusters in the energy range 0.1–2.4 keV. Blue dots are radio relics from the literature (see Ferretti et al. 2012; van Weeren et al. 2019), while the red square shows the location of A1213 in the diagram considering the new X-ray luminosity derived in this work. The figure shows that the diffuse source of A1213 is in agreement with the relic power-cluster X-ray luminosity correlation.

8. Summary and discussion

The mass estimates based both on the optical and the X-ray data confirm that A1213 is a poor galaxy cluster ($M_{200} \sim 2 \times 10^{14} M_{\odot}$). Moreover, we collected convincing evidence that this cluster is far from being dynamically relaxed.

From the optical point of view, despite the fact that the velocity distribution of member galaxies does not deviate significantly from the Gaussianity, a compelling argument in favor of a disturbed dynamics in A1213 comes from the very significant peculiar velocity of the BCG. This is quite unusual in reg-

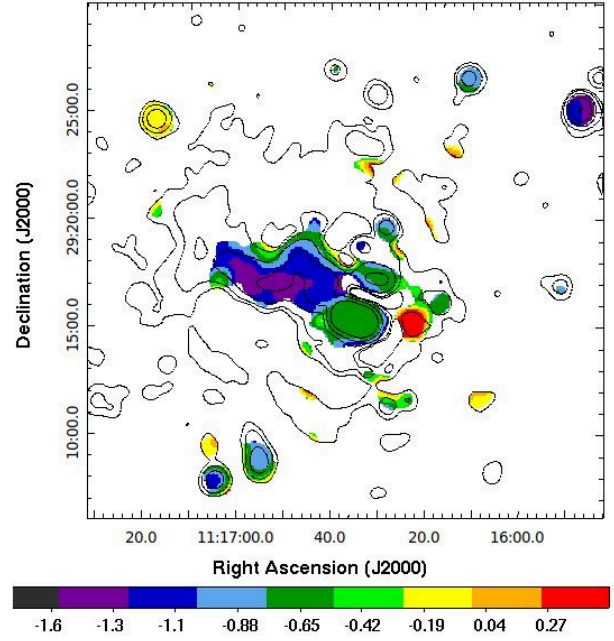


Fig. 15. VLA 1.4 GHz/LOFAR 144 MHz spectral index map of the radio emission of A1213 at the angular resolution of $40'' \times 40''$. As a reference, we also plot in black the contours of the LOFAR image at the same resolution. Contour levels are at 0.84, 3.36, 13.44, 53.76, and $215.04 \text{ mJy beam}^{-1}$.

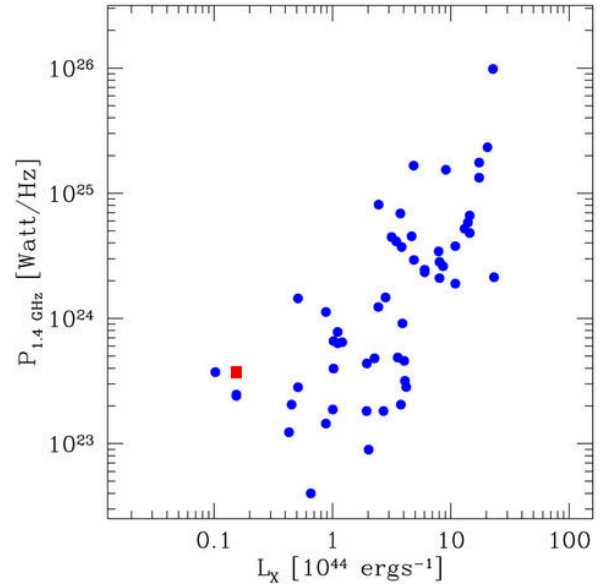


Fig. 16. Monochromatic radio power of relics at 1.4 GHz versus the cluster X-ray luminosity of the parent clusters (energy band 0.1–2.4 keV). Blue dots are radio relics from the literature (see text), while the red square refers to A1213.

ular clusters, where the brightest galaxy is located at the peak of the velocity distribution (see, e.g., the case of CL1821+643; Boschini & Girardi 2018).

With regard to the 2D analysis of the galaxy distribution, we can see that the cluster is only slightly elliptical and roughly oriented in the NE–SW direction. Our analysis of optical substructures suggests that A1213 is composed by several galaxy groups. In particular, we detected two external (at $R \sim R_{200}$) groups: 2D–NW and 2D–NE (see Table 3). 2D–NW is the densest one

and exhibits a dominant galaxy (ID 274) and several galaxies all around, thus maybe it has not yet crossed the central region of A1213. On the contrary, 2D–NE seems elongated in the same direction as the X-ray emission (see below). It could be a group in a recent, post-merger phase occurring in the plane of the sky.

About the central cluster region, both the velocity gradient and the DSV test suggest the existence of two substructures oriented in the NE–SW direction. The one with lower radial velocity is detected also by the 3D–DEDICA test (3D–CORE in Table 4). Indeed, the core of A1213 is quite intricate. The existence of the BCG and the bright couple BG1+BG2, which differ substantially in terms of radial velocity ($\geq 1000 \text{ km s}^{-1}$), could suggest that these galaxies trace a merger almost along the line of sight. In fact, during a merger of two groups, the external galaxies are usually swept away and only the dense cores survive (see simulations by, e.g., González-Casado et al. 1994; Vijayaraghavan et al. 2015). However, if the groups did not have compact cores but rather their luminosity was concentrated in a bright dominant galaxy (or a couple of bright galaxies), the merger is not visible as a double peak in the velocity distribution and it is traced only by the brightest galaxies.

Another important piece of evidence is the fact that blue, star-forming galaxies (e.g., galaxy ID 441 in Table 1) are not restricted to the peripheral regions of the cluster, as shown from the projected phase space of cluster galaxies (Fig. 2). This is not what is commonly found in galaxy clusters, where blue galaxies usually tend to avoid the core regions (e.g., Girardi et al. 2015; Mercurio et al. 2021) and is consistent with the scenario of an assembling cluster through accretion of several poor groups rich in late-type galaxies. Another explanation could be that in A1213, which is a poor cluster, the ram-pressure by the ions of the ICM (see Boselli et al. 2022 for a recent review) is not efficient to quench the star formation in blue galaxies falling into the cluster core.

As for the X-ray properties of A1213, it displays a patchy, shallow X-ray emission on scales of $\sim 700 \text{ kpc}$ (see Fig. 11) in the presence of various point sources. A comparison with Fig. 3 shows that several of these sources coincide with the most prominent optical galaxies in the field, such as BCG, BG1, and ID 442. None of these bright galaxies coincide with the centroid of the X-ray emission. Once the point sources detected in the image are excised, the diffuse X-ray emission appears almost regular, slightly elongated in the NE–SW direction, with an ellipticity of $\epsilon \sim 0.1$ and $\text{PA} \sim 35^\circ$ within $0.5 R_{500}$.

To describe the morphological state of A1213 in the X-ray band, two parameters are useful: the surface brightness concentration c_{SB} and the centroid shift w (see Santos et al. 2008; Poole et al. 2006; Maughan et al. 2008 for details). Since a central surface brightness excess is a primary indicator of the presence of a cool core (Fabian et al. 1984), then the c_{SB} parameter is a useful indicator of the dynamical state of the cluster. On the other hand, the w parameter is sensitive to the presence of bright substructures. For A1213, we derive $c_{\text{SB}} = 0.14$ and $w = 0.025$, a clear indication of this cluster to be unrelaxed. In fact, typical values for disturbed clusters are $c_{\text{SB}} < 0.19$ and $w > 0.01$, as found by Campitiello et al. (2022).

In summary, the diffuse X-ray emission overlaps with the optical galaxy distribution and is slightly elongated in the same NE–SW direction. Moreover, the X-ray morphology, the absence of well-defined emission peaks and the above-defined dynamical indicators strengthen the evidence that A1213 is in an unrelaxed dynamical state. We also note that although the diffuse X-ray emission within R_{500} is clumpy (Fig. 11), its large-scale shape appears only slightly elongated. This indicates that if the cluster

core had a recent interaction it probably did not occur on the plane of the sky.

About the X-ray luminosity of A1213, it was previously proposed that the cluster is underluminous to explain the discrepancy with the power of the radio halo (G09, Giovannini et al. 2011). Considering our new estimate of the luminosity within R_{500} , together with the value of the gas temperature derived through the spectral analysis (see Sect. 6.1), we can now claim that A1213 is not an underluminous cluster (e.g., Lovisari et al. 2021, their Fig. 3). Instead, we determine that it is quite a typical poor cluster.

The purpose of our work was to characterize the optical/X-ray/radio properties of A1213 in order to study the environment of the diffuse radio emission discovered by G09 in this cluster and shed new light on its nature. The SDSS and *XMM-Newton* data show a good agreement in the cluster central region, including the fact that both data sets indicate an elongation in the NE–SW direction. Instead, the observed radio emission does not coincide with the diffuse X-ray emission (see Fig. 3), as occurs generally in unrelaxed clusters with radio halos (e.g., Govoni et al. 2001), because of its offset with respect to the ICM distribution and its extension toward the NE, the same direction traced by the galaxy distribution from the core to the cluster periphery (at $R \sim R_{200}$).

Indeed, recent LOFAR images at 144 MHz of the LoTSS-DR2 confirmed the presence of the diffuse emission observed in A1213 at higher frequencies (see Hoang et al. 2022, their Fig. 4, as well as our Fig. 14). However, since the radio emission does not follow the X-ray emission, (Hoang et al. 2022) infer that this extended source is not a radio halo, but it is the tail of the central radio galaxy 4C29.41 (our ID 467 = BG1) bent by the interaction with the ICM (see their Fig. 4). This would explain why A1213 is an outlier in the normal scale relations between X-ray and radio properties of radio-halo clusters (e.g., Cassano et al. 2013). But the scenario could be even more complicated. In fact, (Hoang et al. 2022) detect an excess of diffuse emission on the easternmost region of the emission seen with LOFAR (see their Fig. 4, left panel). Since there is no obvious optical counterpart of this source, its origin is unclear and these authors propose that it could be associated to a merger occurring in the NE–SW direction.

Our VLA 1.4 GHz/LOFAR 144 MHz spectral index map rejects the hypothesis of the radio galaxy tail and supports a different explanation. In fact, the spectral index distribution (Sect. 7 and Fig. 15) is compatible with a radio relic interpretation, where “fossil” electrons of the radio galaxy 4C29.41 (but also of the head-tail galaxy ID 442) are reaccelerated by shock(s) due to a merger. The radio relic is elongated from the cluster center toward the cluster periphery, therefore it is located either in front or behind the cluster. This is consistent with a merger in the N–S or NE–SW directions, in agreement with the results of our optical analysis. A relic with a similar structure is detected in the cluster Abell 115 (Govoni et al. 2001; Botteon et al. 2016), although the latter is much larger in size. The relic hypothesis is also supported by the plot shown in Fig. 16, where the diffuse source of A1213 fits the empirical correlation between the power of radio relics and the X-ray luminosity of the parent clusters.

Finally, Fig. 14 shows some evidence of fragmented diffuse radio emissions at the cluster center whose nature is uncertain. They could be related to the relic, or could be the tip of the iceberg of very low-surface-brightness emission permeating the cluster center. Indeed, our estimate of the central magnetic field strength, $\langle B_0 \rangle \sim 2\text{--}3 \mu\text{G}$ (Sect. 6.1), is compatible with the possible presence of a faint radio halo in the

cluster core (e.g., van Weeren et al. 2019). Also, recent works (e.g., Hoang et al. 2021; Botteon et al. 2021) reported the discovery with LOFAR of radio halos in low-mass ($M_{500} \lesssim 5 \times 10^{14} M_{\odot}$) galaxy clusters. Thus, the existence of a faint halo in A1213 ($M_{500} \sim 1 \times 10^{14} M_{\odot}$), while quite uncommon, would not be so extraordinary.

In conclusion, A1213 represents an interesting target to investigate the connection between optical (galaxy population) and X-ray (ICM) cluster properties and diffuse radio emissions in a low-mass regime that is still mostly unexplored. In this context, new deeper X-ray observations of this cluster could be decisive to test the proposed relic scenario. In fact, the eventual detection of X-ray surface brightness discontinuities (associated with shocks in the ICM) in correspondence to the suspected radio relic would strengthen our interpretation. Instead, dedicated LOFAR LBA observations (e.g., de Gasperin et al. 2021) could be crucial in characterizing the very low-surface-brightness diffuse emission detected in the center of the cluster.

Acknowledgements. We thank the anonymous referee for his/her useful comments and suggestions. V.V. acknowledges support from Istituto Nazionale di Astrofisica (INAF) mainstream project “Galaxy Cluster Science with LOFAR” 1.05.01.86.05. This research has made use of the galaxy catalog of the Sloan Digital Sky Survey (SDSS). Funding for the SDSS has been provided by the Alfred P. Sloan Foundation, the US Department of Energy Office of Science, and the Participating Institutions. SDSS acknowledges support and resources from the Center for High-Performance Computing at the University of Utah. The SDSS website is <http://www.sdss.org/>, where the complete list of the funding organizations and collaborating institutions can be found. This paper is also based on archival observations obtained with *XMM-Newton*, an ESA science mission with instruments and contributions directly funded by ESA Member States and the USA (NASA). This paper is based in part on data obtained with the International LOFAR Telescope (ILT) under project code LT10_010. LOFAR (van Harlem et al. 2013) is the LOw Frequency ARray designed and constructed by ASTRON. It has observing, data processing, and data storage facilities in several countries, which are owned by various parties (each with their own funding sources), and which are collectively operated by the ILT foundation under a joint scientific policy. The ILT resources have benefited from the following recent major funding sources: CNRS-INSU, Observatoire de Paris and Université d’Orléans, France; BMBF, MIWF-NRW, MPG, Germany; Science Foundation Ireland (SFI), Department of Business, Enterprise and Innovation (DBEI), Ireland; NWO, The Netherlands; The Science and Technology Facilities Council, UK; Ministry of Science and Higher Education, Poland; The Istituto Nazionale di Astrofisica (INAF), Italy. This research made use of the Dutch national e-infrastructure with support of the SURF Cooperative (e-infra 180169) and the LOFAR e-infra group. The Jülich LOFAR Long Term Archive and the German LOFAR network are both coordinated and operated by the Jülich Supercomputing Centre (JSC), and computing resources on the supercomputer JUWELS at JSC were provided by the Gauss Centre for Supercomputing e.V. (grant CHTB00) through the John von Neumann Institute for Computing (NIC). This research made use of the University of Hertfordshire high-performance computing facility and the LOFAR-UK computing facility located at the University of Hertfordshire and supported by STFC [ST/P000096/1], and of the Italian LOFAR IT computing infrastructure supported and operated by INAF, and by the Physics Department of Turin university (under an agreement with Consorzio Interuniversitario per la Fisica Spaziale) at the C3S Supercomputing Centre, Italy.

References

Abell, G. O., Corwin, H. G., Jr., & Olowin, R. P. 1989, *ApJS*, 70, 1
 Arnaud, M., Pointecouteau, E., & Pratt, G. W. 2005, *A&A*, 441, 893
 Asplund, M., Grevesse, N., Sauval, A. J., & Scott, P. 2009, *ARA&A*, 47, 481
 Balestra, I., Mercurio, A., Sartoris, B., et al. 2016, *ApJS*, 224, 33
 Bardelli, S., Pisani, A., Ramella, M., Zucca, E., & Zamorani, G. 1998, *MNRAS*, 300, 598
 Beers, T. C., Flynn, K., & Gebhardt, K. 1990, *AJ*, 100, 32
 Ben Bekhti, N., Flöer, L., Keller, R., et al. 2016, *A&A*, 594, A116
 Bird, C. M., & Beers, T. C. 1993, *AJ*, 105, 1596
 Biviano, A., Katgert, P., Thomas, T., & Adami, C. 2002, *A&A*, 387, 8
 Boschin, W., & Girardi, M. 2018, *MNRAS*, 480, 1187
 Boschin, W., Girardi, M., Barena, R., & Nonino, M. 2012, *A&A*, 540, A43

Boschin, W., Girardi, M., & Gastaldello, F. 2020, *MNRAS*, 492, 2405
 Boselli, A., Fossati, M., & Sun, M. 2022, *A&ARv*, 30, 3
 Botteon, A., Gastaldello, F., Brunetti, G., & Dallacasa, D. 2016, *MNRAS*, 460, L84
 Botteon, A., Cassano, R., van Weeren, R. J., et al. 2021, *ApJ*, 914, L29
 Campitiello, M. G., Etori, S., Lovisari, L., et al. 2022, *A&A*, 665, A117
 Carter, D., & Metcalfe, N. 1980, *MNRAS*, 191, 325
 Cassano, R., Etori, S., Brunetti, G., et al. 2013, *ApJ*, 777, 141
 Cavaliere, A., & Fusco-Femiano, R. 1976, *A&A*, 49, 137
 Condon, J. J., Cotton, W. D., Greisen, E. W., et al. 1998, *AJ*, 115, 1693
 Cuciti, V., Cassano, R., Brunetti, G., et al. 2021, *A&A*, 647, A51
 Danese, L., de Zotti, G., & di Tullio, G. 1980, *A&A*, 82, 322
 de Gasperin, F., Williams, W. L., Best, P., et al. 2021, *A&A*, 648, A104
 den Hartog, R., & Katgert, P. 1996, *MNRAS*, 279, 349
 Dressler, A., & Shectman, S. A. 1988, *AJ*, 95, 985
 Eckert, D. 2016, Astrophysics Source Code Library [record ascl:1608.011]
 Eckert, D. 2020, <https://pyproffit.readthedocs.io/en/latest/index.html>
 Einasto, M., Einasto, J., Tago, E., Müller, V., & Andernach, H. 2001, *AJ*, 122, 2222
 Etori, S., Gastaldello, F., & Leccardi, A. 2010, *A&A*, 524, A68
 Fabian, A. C., Nulsen, P. E. J., & Canizares, C. R. 1984, *Nature*, 310, 733
 Fadda, D., Girardi, M., Giuricin, G., Mardirossian, F., & Mezzetti, M. 1996, *ApJ*, 473, 670
 Feretti, L., Orrù, E., Brunetti, G., et al. 2004, *A&A*, 423, 111
 Feretti, L., Giovannini, G., Govoni, F., & Murgia, M. 2012, *A&ARv*, 20, 54
 Gebhardt, K., & Beers, T. C. 1991, *ApJ*, 383, 72
 Ghirardini, V., Eckert, D., Etori, S., et al. 2019, *A&A*, 621, A41
 Giovannini, G., Bonafede, A., Feretti, L., et al. 2009, *A&A*, 507, 1257
 Giovannini, G., Feretti, L., Girardi, M., et al. 2011, *A&A*, 530, L5
 Girardi, M., & Biviano, A. 2002, *Astrophys. Space Sci. Lib.*, 272, 39
 Girardi, M., Fadda, D., Giuricin, G., et al. 1996, *ApJ*, 457, 61
 Girardi, M., Mercurio, A., Balestra, I., et al. 2015, *A&A*, 579, A4
 Girardi, M., Boschin, W., Gastaldello, F., et al. 2016, *MNRAS*, 456, 2829
 González-Casado, G., Mamon, G. A., & Salvador-Solé, E. 1994, *ApJ*, 433, 61
 Govoni, F., Feretti, L., Giovannini, G., et al. 2001, *A&A*, 376, 803
 Govoni, F., Murgia, M., Vacca, V., et al. 2017, *A&A*, 603, A122
 Hernández-Fernández, J. D., Iglesias-Páramo, J., & Vílchez, J. M. 2012, *ApJS*, 199, 2
 Hoang, D. N., Shimwell, T. W., Osinga, E., et al. 2021, *MNRAS*, 501, 576
 Hoang, D. N., Brüggén, M., Botteon, A., et al. 2022, *A&A*, 665, A60
 Lauer, T. R., Postman, M., Strauss, M. A., Graves, G. J., & Chisari, N. E. 2014, *ApJ*, 797, 82
 Leccardi, A., & Molendi, S. 2008, *A&A*, 486, 359
 Ledlow, M. J., Voges, W., Owen, F. N., & Burns, J. O. 2003, *AJ*, 126, 2740
 Lovisari, L., Etori, S., Gaspari, M., & Giles, P. A. 2021, *Universe*, 7, 139
 Maughan, B. J., Jones, C., Forman, W., & Van Speybroeck, L. 2008, *ApJS*, 174, 117
 Mercurio, A., Rosati, P., Biviano, A., et al. 2021, *A&A*, 656, A147
 Munari, E., Biviano, A., Borgani, S., Murante, G., & Fabjan, D. 2013, *MNRAS*, 430, 2638
 NAG Fortran Workstation Handbook 1986, *NAG Fortran Workstation Handbook* (Downers Grove, IL: Numerical Algorithms Group)
 Navarro, J. F., Frenk, C. S., & White, S. D. M. 1997, *ApJ*, 490, 493
 Pisani, A. 1993, *MNRAS*, 265, 706
 Pisani, A. 1996, *MNRAS*, 278, 697
 Plionis, M. 2002, *MNRAS*, 329, L47
 Poole, G. B., Fardal, M. A., Babul, A., et al. 2006, *MNRAS*, 373, 881
 Rood, H. J., & Sastry, G. N. 1971, *PASP*, 83, 313
 Santos, J. S., Rosati, P., Tozzi, P., et al. 2008, *A&A*, 483, 35
 Shimwell, T. W., Hardcastle, M. J., Tasse, C., et al. 2022, *A&A*, 659, A1
 Silverman, B. W. 1986, *Density Estimation for Statistics and Data Analysis* (London: Chapman and Hall/CRC)
 Smith, R. K., Brickhouse, N. S., Liedahl, D. A., & Raymond, J. C. 2001, *ApJ*, 556, L91
 Snowden, S. L., Mushotzky, R. F., Kuntz, K. D., & Davis, D. S. 2008, *A&A*, 478, 615
 Turner, M. J. L., Abbey, A., Arnaud, M., et al. 2001, *A&A*, 365, L27
 Vacca, V., Shimwell, T., Perley, R. A., et al. 2022a, *MNRAS*, 511, 3389
 Vacca, V., Govoni, F., Murgia, M., et al. 2022b, *MNRAS*, 514, 4969
 van Harlem, M. P., Wise, M. W., Gunst, A. W., et al. 2013, *A&A*, 556, A2
 van Weeren, R. J., Röttgering, H. J. A., Brüggén, M., & Hoefl, M. 2010, *Science*, 330, 347
 van Weeren, R. J., de Gasperin, F., Akamatsu, H., et al. 2019, *Space. Sci. Rev.*, 215, 16
 Vijayaraghavan, R., Gallagher, J. S., & Ricker, P. M. 2015, *MNRAS*, 447, 3623
 Yuan, Z. S., Han, J. L., & Wen, Z. L. 2015, *ApJ*, 813, 77